Article:
Zhang, G., Ma, L. and Pourkashanian, M. (2023) A porous medium approach to the 3D modelling of an entire rotating packed bed for post-combustion carbon capture. Chemical Engineering Science, 274. 118687. ISSN: 0009-2509

https://doi.org/10.1016/j.ces.2023.118687

A porous medium approach to the 3D modelling of an entire rotating packed bed for post-combustion carbon capture

Guojun Zhang, Lin Ma*, Mohamed Pourkashanian

Energy 2050, Mechanical Engineering, Faculty of Engineering, University of Sheffield, Sheffield S10 2TN, UK

Abstract: Rotating packed bed (RPB) technology shows great potential for post-combustion capture. However, the capture process inside the full RPB is difficult to simulate, due to the complexity of the process and the neglect of the CO_2 capture in the outer cavity zone. In this paper, a full 3D CFD model, including the packing and the inner and outer cavity zones, has been established employing the Eulerian porous medium method coupled with various sub-models. The CO_2 capture performance in the packing and outer cavity zones has been quantitatively analyzed under different operating conditions. The simulation results show good agreement with the experimental data, and the contribution of the outer cavity zone to the CO_2 capture of the RPB is in the range of 28%~42%. This work provides a new approach to efficiently simulate the mass transfer process in the RPB.

Keywords: rotating packed bed, Eulerian method, 3D porous media model, CO_2 absorption, outer cavity zone

Nomenclatures

a_S	specific area of the packing materials, $m^2 \cdot m^{-3}$	$S_{h,i}$	heat of chemical reaction, $W \cdot m^{-3}$
A_e	effective interfacial area, $m^2 \cdot m^{-3}$	$\vec{S}_{GL}$	interfacial force between the gas and liquid phases, $N \cdot m^{-3}$
C	concentration, $kmol \cdot m^{-3}$	t	time, s
C_{pG}	specific heat of gas phase, $J \cdot kg^{-1} \cdot K^{-1}$	T_i	temperature of phase *i*, K
C_D	drag coefficient	u	flow rate per unit area, $m \cdot s^{-1}$
D	diffusivity, $m^2 \cdot s^{-1}$	$\vec{u}_i$	velocity of phase *i*, $m \cdot s^{-1}$
E	enhancement factor	V	volume, m^3
E_i'	total energy, J	We	Weber number
f , f^*	drag function	x	radial length of a cell, m
f_e	ratio of wetted packing area to the total packing surface area	y_{i,CO_2} , y_{o,CO_2}, y_{op,CO_2}	CO_2 mole fraction in the gas inlet and outlet and on the outer packing surface, respectively
$\vec{F}_{disp,i}$	dispersion forces of phase *i*, $N \cdot m^{-3}$	Y	mass fraction of species
$\vec{F}_{drag,i}$	interaction force between the phase *i* and solids of the packing material, $N \cdot m^{-3}$	*Greek*	
g	gravitational force, $m \cdot s^{-2}$	α	phase saturation
h	height of the packing, m	γ	packing void fraction (porosity)
h_j	enthalpy of the species, $J \cdot mol^{-1}$	β	dynamic contact angle, °
h_{GL}	heat transfer coefficient between the gas and liquid phases, $W \cdot m^{-2} \cdot K^{-1}$	ε	volume fraction
H	Henry constant	δ	diffusion layer thickness, m
Ha	Hatta number	ω	angular velocity, $rad \cdot s^{-1}$
$\vec{J}$	mass diffusion flux of species, $kg \cdot m^{-2} \cdot s^{-1}$	κ_G	thermal conductivity of the gas phase, $W \cdot m^{-1} \cdot K^{-1}$
k_i'	thermal conductivity, $W \cdot m^{-1} \cdot K^{-1}$	θ	angle of flow direction slop to the bed axis, °
k_i	mass transfer coefficient of phase *i*, $m \cdot s^{-1}$	ρ_i	density of phase *i*, $kg \cdot m^{-3}$
k_2	reaction rate constant, $m^3 \cdot mol^{-1} \cdot s^{-1}$	$\Delta\rho_{GL}$	absolute value of the density difference between liquid and gas phases, $kg \cdot m^{-3}$
K_L	overall mass transfer coefficient, $m \cdot s^{-1}$	μ	dynamic viscosity, $kg \cdot m^{-1} \cdot s^{-1}$

K_{GL}	momentum exchange coefficient between the gas and liquid phases	μ_e	effective dynamic viscosity, $kg \cdot m^{-1} \cdot s^{-1}$
$K_L a_e$	overall volumetric mass transfer coefficient, s^{-1}	τ	particulate relaxation time, s
M	molar mass, $g \cdot mol^{-1}$	$\bar{\bar{\tau}}$	stress tensor, $N \cdot m^{-2}$
N_{CO_2}	transfered CO_2 between the gas and liquid, $kg \cdot m^{-1} \cdot s^{-1}$	$\bar{\bar{\tau}}_{eff,ij}$	effective shear tensor
Nu	Nusselt number	λ_{RT}	Rayleigh-Taylor instability wavelength
P	pressure, Pa	σ	surface tension, $N \cdot m^{-1}$
P_c	capillary pressure, Pa	ν	kinematic viscosity, $m^2 \cdot s^{-1}$
Pr	Prandtl number	*Subscripts*	
q	liquid initial velocity number	*cell*	mesh cell
Q	volume flow rate, $m^3 \cdot s^{-1}$	*CO2*	carbon dioxide
$Q_{h,GL}$	transferred heat between the gas and liquid phases, $W \cdot m^{-3}$	*G*	gas phase
r	radius or radial distance, m	*i*	=G, L
r_i	inner packing radius, m	*j*	species
r_o	outer packing radius, m	*L*	liquid phase
r_{CO_2}	CO_2 reaction rate, $kg \cdot m^{-3} \cdot s^{-1}$	*MEA*	monoethanolamine
R	gas constant	*O*	outer cavity zone
R_{ij}	net rate of production of the species *j* by the reaction, $mol \cdot m^{-3} \cdot s^{-1}$	*OW*	computational cell next to the casing wall
Re	Reynolds number	*P*	packing zone
Re'	relative Reynolds number	*PW*	computational cell next to the packing wall
$S_{m,i}$	mass transfer rate between gas and liquid, $kg \cdot m^{-3} \cdot s^{-1}$	*S*	solids phase for the packing materials

1. Introduction

CO_2 emissions, as a kind of greenhouse gas, has become an urgent issue in the 21st century (Khan, 2017). In response to this important issue, the EU has a commitment for a net-zero greenhouse gas emissions target by 2050 (Garba, 2012), which aims to reach a balance between the amount of greenhouse gas emissions produced and the amount captured. Particularly, the total power plants contribute a huge amount of CO_2, which could contribute to 30% of the total CO_2 emissions. Therefore, reducing CO_2 emissions released by the power stations has become an emergent activity.

Currently, the amine-based post-combustion CO_2 capture (PCC) is the most common and commercial way to capture CO_2 using the conventional packed bed (CPB), which results in the CPB being large and costly. In addition, the high amine solvent flow rate demanded by the large CPB would consume large heat energy for the rich solvent regeneration. On the other hand, the rotating packed bed (RPB), one of the most important applications in the area of process intensification, has the potential to enhance the CO_2 capture performance and reduce the packed bed size by applying a high centrifugal force (100-1000 times gravity) (Liu et al., 2019). However, the RPB is on the early stage of the technological development for PCC, and the CO_2 capture processes, including the hydrodynamics, heat and mass transfer, are still unclear inside a RPB. Thus, it requires extensive research and design optimization.

In general, the RPB may be divided into three parts - inner cavity, packing and outer cavity zones, see Figure 1. At the beginning, the liquid jets out from the liquid distributor and passes through the inner cavity zone entering the packing region, then the liquid contacts and reacts with the opposing gas flow on its way outwards through the packing region. During this process, the liquid breaks into tiny droplets, or generates thin films on the packing surface due to the strong interaction with the rotating mesh packing, which can enhance the interfacial area and micromixing (Yang et al., 2015b) between gas and liquid. In addition, the liquid surface renewal rate in the packed bed is improved, which also leads to a large increase in the CO_2 capture. In addition, the liquid leaves the packing with a large tangential velocity and enters the outer cavity zone in the form of liquid droplets. Finally, the liquid droplets hit the cavity casing wall and the liquid phase flows out from the liquid outlet tube under the influence of the gravitational force. It should be noted that before the liquid leaves the outlet tube, the liquid has been reacting with the gas phase all the time in the outer cavity zone. In addition, the space ratio of the outer cavity zone to the packing region is large (Guo et al., 2019). As a result, it can be concluded that the CO_2 capture in the RPB occurs not only in the packing zone, but also in the outer cavity zone.

However, most investigations only focus on the packing region, the contribution of the outer cavity zone for the CO_2 capture is rarely studied. In the experimental investigations, it has been reported that the effective interfacial area of the outer cavity zone could be up to 30% of the entire effective area (Guo et al., 2014; Sang et al., 2017a). Further, experiments showed that the contribution of the outer cavity zone to the mass transfer was determined to take up approximately 13–25% of the total mass transfer in the entire RPB (Sang et al., 2019; Yang et al., 2011). Therefore, the CO_2 absorption in the outer cavity zone cannot be ignored.

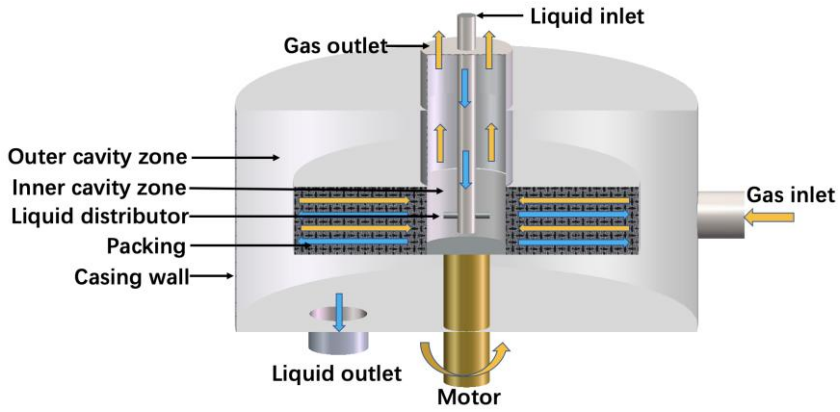

Figure 1. Schematic diagram of a typical RPB for CO_2 capture.

In addition, the Volume of Fraction (VOF) method has widely used to computationally study the CO_2 capture in the RPBs. For instance, the micromixing and mass transfer have been studied in a 2D packing region along with the Volume of Fraction (VOF) method and user defined functions (UDF) (Guo et al., 2016; Yang et al., 2016). The advantage of employing the VOF method is that it can reasonably, clearly and accurately capture the interface between the gas and liquid, including the evolution of the liquid droplets in the RPB. Due to the multiscale nature of the liquid flow in an RPB, the computational mesh should be fine enough to resolve the finest droplet and liquid films, typically in millimeter and even micron meter scales, in addition to the packings, within a meter scale RPB. When modelling in 3D this will require a prohibitively large number of computational cells and computational time. This is the reason why most of

78 the CFD simulations using CFD methods are for small RPB models and mostly in 2D.
79 If the packing in an RPB is treated as a porous medium using the Eulerian model, where
80 the liquid flow is modelled as a continuum, there is no need to resolve the packing or
81 the liquid droplets. Instead, the interfacial area and the momentum transfer between the
82 phases are modelled using experimental correlations. Clearly, this method could not
83 produce a clear picture of the real discrete liquid droplet flow and its accuracy relies on
84 correlations employed for the resistance among the phases and the interfacial area.
85 Nevertheless, the Eulerian method could significantly reduce the simulation time and
86 with appropriate validations, it can potentially be utilized to address the significant
87 difficulties of modelling 3D and large-scale RPBs (Lu et al., 2019; Zhang et al., 2022a).

88 However, the Eulerian porous medium approach has so far seldom been employed for
89 the RPB because the momentum transfer between the phases has to be closed by closure
90 equations. In other words, a suite of mathematical formulations is essential for
91 accurately expressing the flow characteristics in the RPB, such as the sub-models for
92 the forces for the phases and the effective interfacial area between the phases (Fourati
93 et al., 2013; Iliuta et al., 2014). Since the characteristics of the multiphase flow are very
94 different when passing through the rotating packing and in the static cavity space, sub-
95 models for the forces and the interfacial area should be separately introduced for the
96 packing region and the outer cavity zone, which is quite complex. For the packing
97 region, not only the porous resistance should be considered due to the wire mesh
98 packing, but also the dispersion force should be taken into account due to the strong
99 interaction between the liquid and the packing (Jiang et al., 2002; Xu et al., 2019; Zhang
100 et al., 2022b). In addition, it is complex to predict the contact area between gas and
101 liquid due to the non-uniform liquid distribution in the packing zone. The above force
102 and the effective mass transfer area models for the non-uniform multiphase flow in the
103 packing zone have been developed and validated in our previous paper (Zhang et al.,
104 2022a). However, for the outer cavity zone, the liquid phase exists in the form of liquid
105 droplets in the cavity space and liquid film on the casing wall. As a result, different

contact area correlations for the liquid droplets and film should be proposed. In addition, there is no existing force models for the outer cavity zone via employing the Eulerian method. Therefore, the appropriate model and correlation for the outer cavity zone should be developed for accurately analysing the hydrodynamics in this zone.

In addition to the momentum transfer between phases, the heat and mass transfer should be modelled in the RPB. Many semi-empirical correlations for predicting the mass transfer coefficients have been proposed in the literature based on different applications and packing systems of the RPBs (Munjal et al., 1989), however, these correlations are too general to be confidently employed for the CO_2-MEA absorption system employed (Lu et al., 2019). A method that has been commonly used to model the chemically-enhanced mass transfer in the CPB, is to use an enhancement factor coupled with a mass transfer theory, such as the two-film, penetration, or surface renewal theories. Although penetration and surface renewal theories are more accurate in calculating the mass transfer by introducing the contact time and surface renewal frequency, these two parameters are difficult to measure in the RPB, especially under unsteady-state conditions. Furthermore, the two-film reaction-enhanced mass transfer model has already shown sufficient accuracy for expressing the CO_2 mass transfer among the phases in many CPB investigations (Dashliborun et al., 2019; Kim et al., 2017; Pham et al., 2015), which is introduced into the RPB model as presented in Sections 2.4 and 2.5.

The thermodynamics in the RPB should also be carefully considered because the liquid temperature and the chemical reaction rate could affect each other in this CO_2 chemisorption system. The heat released by the chemical reaction increases the liquid temperature; meanwhile, some of the heat would be carried away by the gas flow due to the temperature difference between the phases so that the gas temperature also increases. The increasing phase temperature would speed up the reaction rate until the whole CO_2 absorption system reaches a balance. In particular, the efficiency of the heat

transfer between the phases is determined by the diameter of the liquid droplet. The smaller the droplet diameter, the more heat transfer takes place. The predicted heat and mass transfer processes can be made accurate only when the liquid droplet diameters in the packing and outer cavity zones are set properly.

In our previous work, the CO_2 capture performance in the RPB was explored in a 2D packing region by the Eulerian porous medium method (Lu et al., 2019). However, the predicted liquid outlet temperature and the overall volumetric mass transfer rate ($K_L a_e$), which was defined in Section 3.3, were lower than the experimental data because the outer cavity zone was not taken into consideration at the time and the liquid droplet diameter was set using the default value in the software. In this paper, for accurately studying the CO_2 capture process within a RPB, a comprehensive 3D RPB model, including the packing, inner and outer cavity zones, was built based on a practical pilot-scale RPB coupled with various sub-models. The $K_L a_e$ and liquid outlet temperature under various operating conditions were analysed. Furthermore, the ratio of the CO_2 capture performance in the packing zone and outer cavity zone was quantitatively investigated. Therefore, this paper provides, for the first time, a new feasible approach to effectively and accurately predict the mass transfer within the entire RPB.

2. CFD simulations

In this section, a 3D model has been built that incorporates the porous resistance, dispersion force, two-film reaction enhancement mass transfer and heat transfer models in order to achieve an accurate prediction of the flow dynamics, mass transfer and heat transfer in the whole RPB. Since the resistance and dispersion models developed for the packing zone have been illustrated in our previous paper (Zhang et al., 2022a), only some of the most important models and equations, such as the governing equations, mass and heat transfer models, and the correlations of the effective interfacial area and liquid droplet diameter, are presented in this paper.

2.1 Geometry of the RPB

In order to establish and validate the 3D RPB model, the detailed information of the experimental rig and the quality of the experimental results are required. Among all the published experimental works on RPBs, the Kolawole experimental data (Kolawole, 2019) has been selected as the comparison data. The reasons are: (i) the relative detailed operating conditions and dimensions of the RPB have been offered, especially the size of the packing and outer cavity zones. (ii) The CO_2 capture performance with different operational conditions is analyzed by various indexes, including the overall mass transfer coefficient, the liquid and gas phase temperatures at the outlets, etc., which could help to validate the simulation results. And (iii) the experimental data has been presented in the published paper (Lee et al., 2017) and previously utilized by Lu et al. (2019) for verifying their models, thus meaning that the experimental data is reliable. However, no experimental data related to the flow characteristics (i.e. liquid holdup) has been shown in the thesis (Kolawole, 2019), thus, the flow dynamics obtained by the experiment and simulation are not compared in this work.

The 3D RPB geometry has been reproduced in Figure 2 according to the experimental rig (Kolawole, 2019). The inner diameter, outer diameter and height of the wire mesh packing are 80, 300 and 20 mm, respectively, and it is made from stainless steel with an expanded mesh grade 707. The void fraction and specific area of the packing are 0.801 and 663 m^2/m^3, respectively. The diameter and the estimated height of the RPB casing are 360 and 180 mm, respectively and the space ratio of the outer cavity zone to the packing zone is about 11. There are two gas inlet tubes and one liquid inlet tube with diameters of 60 and 14 mm, respectively. In order to make the mesh in the outer cavity tetrahedral and further reduce the mesh number, the shape of the gas inlet tubes and one liquid inlet tube is simplified to be a rectangle but with the same flow cross-sectional area. In addition, a gas outlet tube is outside the liquid inlet tube with a diameter being 40 mm. A 2-arm liquid distributor is used, and its length and diameter are 22.4 and 7 mm, respectively. In Figure 2, only two liquid nozzle outlet holes are presented. In order to save computational time, the liquid flows passing through the

liquid inlet tube and 2-arm liquid distributor has not been modelled. Initially, a liquid pressure outlet boundary was built at the bottom of the RPB to ensure that the liquid phase flows out from the RPB. However, after the simulation, we found that a large amount of the gas phase would flow out from this boundary at the same time. Thus, an elimination zone is employed at the bottom of the RPB to remove the liquid phase but to retain the gas phase, and the appropriate source equations for this zone can be found in (Zhang et al., 2022a).

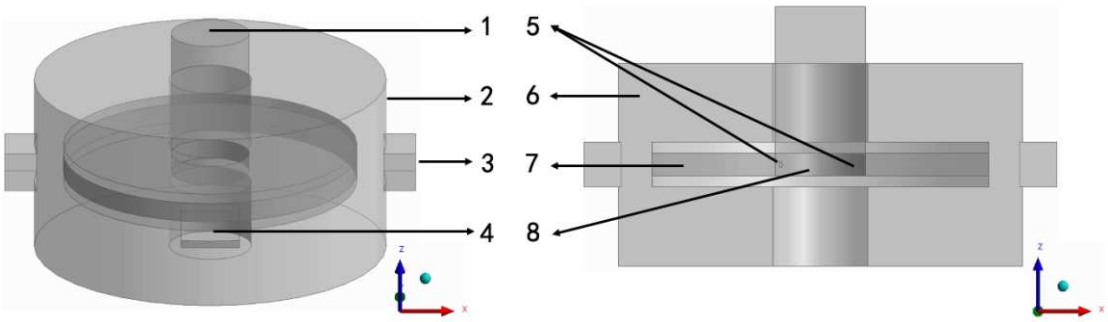

Figure 2. Schematic diagram of the 3D RPB (1, gas outlet; 2, case; 3, gas inlet; 4, liquid elimination zone; 5, liquid inlet; 6, outer cavity zone; 7, packing zone; 8, inner cavity zone).

2.2 Governing fluid flow equations

The main assumptions of the RPB model are as follows:

(i) The wire mesh packed bed is a homogenous porous medium.

(ii) The gas is incompressible.

(iii) The pressure field is shared by the gas and liquid phases.

(iv) The liquid phase exists in the form of the film and droplets in the packing and outer cavity zone.

(v) The mass transfer only happens in the packing and outer cavity zones due to the small interfacial area and short contact time in the inner cavity zone.

(vi) The heat transfer only occurs between the gas and liquid phases and the

casing wall is adiabatic.

The continuity equation utilized to calculate the overall mass conservation is given as follows:

$$\frac{\partial}{\partial t}(\varepsilon_i \rho_i) - \nabla \cdot (\varepsilon_i \rho_i \vec{u}_i) = S_{m,i} \quad (1)$$

where ρ_i is the density of the *i*th phase (*i* = G for gas or L for liquid), t is the time, $\vec{u}_i$ is the phase velocity, $S_{m,i}$ is the mass transfer rate between phases, and ε_i is the phase fraction, which is defined as follows:

$$\varepsilon_i = \alpha_i \gamma = \frac{V_i}{V_G + V_L}\gamma = \frac{V_i}{V_G + V_L + V_S} \quad (2)$$

where α_i is the phase saturation ($\alpha_i = \frac{V_i}{V_G + V_L}$), V_i is the volume of the *i*th phase, and γ and V_S are the porosity and solid volume of the packing, respectively, which are 1 and 0 for the outer cavity zone.

The momentum conservation equations for the packing and outer cavity zones are different since the drag, capillary and mechanical dispersion forces only exist in the packing region. The governing momentum equations for the whole RPB are as follows:

$$\frac{\partial}{\partial t}(\varepsilon_L \rho_G \vec{u}_L) + \nabla \cdot (\varepsilon_L \rho_L \vec{u}_L \vec{u}_L) = -\varepsilon_L \nabla P + \varepsilon_L \nabla P_c + \nabla \cdot (\varepsilon \bar{\bar{\tau}}_L) + \varepsilon_L \rho_L \vec{g} - \vec{F}_{drag,L} + \vec{S}_{GL} + \vec{F}_{disp,L} \quad (3)$$

$$\frac{\partial}{\partial t}(\varepsilon_G \rho_G \vec{u}_G) + \nabla \cdot (\varepsilon_G \rho_G \vec{u}_G \vec{u}_G) = -\varepsilon_G \nabla P + \nabla \cdot (\varepsilon \bar{\bar{\tau}}_G) - \vec{F}_{drag,G} + \varepsilon_G \rho_G \vec{g} - \vec{S}_{GL} + \vec{F}_{disp,G} \quad (4)$$

where P is the pressure, P_c is the capillary pressure, which is produced by the difference in the pressures across the fluid interface and only included in the liquid phase momentum equation, model details please refer to (Zhang et al., 2022a), $\bar{\bar{\tau}}_i$ is the stress tensor, $\vec{F}_{drag,i}$ is the drag force between the phase and packing, $\vec{S}_{GL}$ is the interfacial force between the gas and liquid, and $\vec{F}_{disp,i}$ is the mechanical dispersion force.

The species transport equation and energy equation are shown as follows:

$$\frac{\partial(\varepsilon_i \rho_i \vec{u}_i Y_{ij})}{\partial t} + \nabla \cdot (\varepsilon_i \rho_i \vec{u}_i Y_{ij}) = -\nabla \cdot (\varepsilon_i \vec{J}_{ij}) + \varepsilon_i R_{ij} \quad (5)$$

$$\frac{\partial(\varepsilon_i \rho_i E_i)}{\partial t} + \nabla \cdot \left(\varepsilon_i \vec{u}_i (\rho_i E_i' + P)\right) = \varepsilon_i \nabla P \left(k_i' \nabla T_i - \sum h_j \vec{J}_{ij} + (\bar{\bar{\tau}}_{eff,ij} \cdot \vec{u}_i) \right) + \varepsilon_i Q_{h,i} + \varepsilon_i S_{h,i} \quad (6)$$

where Y_{ij} is the mass fraction of the species *j* in *i*th phase, such as the CO_2 in the gas phase or MEA in the liquid phase (*j*= species), R_{ij} is the production of the species *j* by the reaction, such as MEACOO$^-$ ($HOC_2H_4NHCOO^-$), $\vec{J}_{ij}$ is the mass diffusion flux, E_i' is the total energy, k_i' is the thermal conductivity, h_j is the enthalpy of the species, $\bar{\bar{\tau}}_{eff,ij}$ is the effective shear tensor, $Q_{h,i}$ is the transferred heat between the phases, see Section 2.6, and $S_{h,i}$ is the heat of chemical reaction, which may be obtained by $S_{h,i} = -\sum_j h_j R_{ij}$ (Mardani and Mahalegi, 2019).

2.3 Effective interfacial area and forces

Since the effective gas-liquid interfacial area and forces are quite different between the packing zone and outer cavity zone, the effective interfacial area correlation and force models for these two zones should be separately developed. In the packing region, models for the interfacial, drag and dispersion (including capillary and mechanical dispersion) forces and the effective interfacial area for the non-uniform multiphase flow in the RPB have been introduced in the previous work (Zhang et al., 2022a). It is worth mentioning that the angle between the flow direction and the bed axis (θ) included in the porous resistance model is set as 10°, which is determined by a commonly used specification of the wire meshes with the wire mesh diameter and the centre distance between the wire mesh being 0.6 and 3.5 mm, respectively. Also, this value has been employed in the work of Zhang et al. (2022c). Furthermore, when the dynamic contact angle (β) in the effective interfacial area model is set as 12°, the modelled fractional effective interfacial area for the cases simulated in Section 3 is in a reasonable range of 0.29-0.52 (Luo et al., 2017; Yang et al., 2011) and the CO_2 capture coefficient matches

the experimental data well. In this section, only the effective interfacial area and force model for the outer cavity zone are discussed.

2.3.1 Effective interfacial area model

At present, no correlation of the effective interfacial area has been introduced for the outer cavity zone of the RPBs in the published papers. For a spherical bubble or droplet, the algebraic interfacial area concentration models are derived from the surface area to volume ratio ($A_p = \frac{\pi d_p^2}{\frac{1}{6}\pi d_p^3} = \frac{6}{d_p}$). When using the Eulerian multiphase model, a commonly used equation, as given in Eq. 7, could be utilized to estimate the effective interfacial area, which has been built in Fluent ia-symmetric model.

$$A_{e,O} = \frac{6\varepsilon_G \varepsilon_L}{d_{p,O}} \tag{7}$$

where $A_{e,O}$ is the effective interfacial area in the outer cavity zone, $d_{p,O}$ is the average diameter of the liquid droplets in the outer cavity zone. The ia-symmetric model not only considers the gas and liquid volume fraction, but also takes into account the liquid diameter. In the experimental work of Sang et al. (2017b), they concluded that the liquid exists in the outer cavity zone mainly in the form of droplets and a correlation of the average droplet diameter in the outer cavity zone has been proposed as follows (Sang et al., 2017b):

$$d_{p,O} = 0.042We^{-0.272}Re^{0.068}\left(\frac{u_0}{\omega r_o}\right)^{0.098} r_o \tag{8}$$

$$We = \frac{\rho\omega^2 r_o^3}{\sigma}; Re = \frac{\rho\omega r_o^2}{\mu}; q = \frac{u_0}{\omega r_o};\ u_0 = \frac{Q_L}{2\pi r_i h} \tag{9}$$

where We is the Weber number, Re is the Reynolds number with outer packing radius as the characteristic linear dimension, ω is the angular velocity, Q_L is the liquid volumetric flow rate, σ is the liquid surface tension, μ is the liquid viscosity, and r_o, r_i and h are the outer radius, inner radius and height of the packing, respectively.

Because the liquid on the casing wall exists in the form of the liquid film instead of the liquid droplet, Eq. (7)-(9), which are developed for the liquid droplets in the outer cavity space, cannot be used for estimating the contact area between the gas and the liquid film near the casing wall. If the casing wall surface is fully covered by the liquid film, then the effective interfacial area in the cell next to the casing wall ($a_{e,OW}$) is estimated as follows:

$$A_{e,OW} = \frac{A_{cell,OW}}{V_{cell,OW}} = \frac{1}{\Delta x_{OW}} \tag{10}$$

where $A_{cell,OW}$ and $V_{cell,OW}$ are the wall area surface and volume in the computational cell next to the casing wall, respectively, and Δx_{OW} is the radial length of the cell normal to the casing wall. For the case studied in this paper, the radial length Δx_{OW} is 0.005 m, thus, the effective interfacial area near the casing wall is no more than 200 m^2/m^3. According to Equation (10), it appears that the maximum effective interfacial area ($A_{e,OW}$) depends on Δx_{OW}. Nevertheless, it should be noted that the unit of the interfacial area ($A_{e,OW}$) is m^2/m^3, and therefore it is more suitable to describe $A_{e,OW}$ as the interfacial area concentration. The real physical interfacial area (m^2) could be obtained by $A_{OW} = A_{e,OW}V_{cell,OW} = A_{cell,OW}$, which is independent on the first-layer mesh size at the wall.

In addition, within the packing bed, the method given by (Lu et al., 2019) has been employed to calculate the effective interfacial area in the cell next to the packing wall as follows:

$$A_{e,PW} = \frac{A_{PW}f_e + a_s f_e V_{cell,PW}}{V_{cell,PW}} = \left(\frac{1}{\Delta x_{PW}} + a_s\right) f_e \tag{11}$$

where $A_{cell,PW}$ and $V_{cell,PW}$ are the wall surface area and volume of the cell next to the packing wall, respectively, Δx_{PW} is the radial length of the cell normal to the packing wall, a_s is the specific area of the packing, f_e is the fractional effective interfacial area in the packing, which is the ratio of the wet area to the total packing area ($\frac{A_{e,P}}{a_s}$), and f_e of the packing walls is considered to be the same as that in the packing region.

2.3.2 Interfacial force model

The interfacial force is the only force for the liquid and gas phases in the outer cavity zone. It is due to the momentum exchange between the gas phase and liquid phase and this force is usually presented as an exchange coefficient in Ansys Fluent. There are many built-in models to calculate the interfacial exchange coefficient and a model, named universal drag laws (Ishii and Zuber, 1979), has been designed for the bubble-liquid and droplet-gas flows that could be utilized for modelling the interfacial exchange coefficient in the outer cavity zone, namely

$$K_{GL} = \frac{\varepsilon_G \varepsilon_L \rho_L f}{\tau_L} \tag{12}$$

$$\tau_L = \frac{\rho_L d_p^2}{18\mu_G} \tag{13}$$

$$f = \frac{C_D Re}{24} \tag{14}$$

$$Re' = \frac{\rho_G |\vec{u}_G - \vec{u}_L| d_p}{\mu_e} \tag{15}$$

$$C_D = \begin{cases} \dfrac{24}{Re'} & Re' < 1 \\ \dfrac{24}{Re'}(1 + 0.1Re^{0.75}) & 1 \le Re' \le 1000 \\ \dfrac{2}{3}\left(\dfrac{d_p}{\lambda_{RT}}\right)\left\{\dfrac{1 + 17.67 f^{*6/7}}{18.67 f^*}\right\}^2 & Re' > 1000 \end{cases} \tag{16}$$

$$f^* = (1 - \varepsilon_L)^3;\ \mu_e = \frac{\mu_G}{(1 - \varepsilon_L)^{2.5}};\ \lambda_{RT} = \left(\frac{\sigma}{g \Delta\rho_{GL}}\right)^{0.5} \tag{17}$$

where K_{GL} is the interfacial exchange coefficient, f and f^* are the drag functions, τ_L is the particulate relaxation time, C_D is the drag coefficient, Re' is the relative Reynolds number, μ_e is the effective viscosity, λ_{RT} is the Rayleigh-Taylor instability wavelength, g is the gravity, and $\Delta\rho_{GL}$ is the absolute value of the density difference between liquid and gas phases.

2.4 Mass transfer rate model

The two-film theory has by far been the most popular and useful theory for dealing with the CO_2 mass transfer among the phases (Gbadago et al., 2020; Kim et al., 2016, 2017; Pham et al., 2015). Generally, based on the two-film model and the Henry law, the overall mass transfer coefficient and enhancement factor are applied to model the CO_2 mass transfer between the gas phase and MEA solution, which can be expressed as follows:

$$N_{CO_2} = K_L A_e \left(C^*_{CO_2} - C_{CO_2}\right) \tag{18}$$

$$\frac{1}{K_L} = \frac{RT}{H_{CO_2-MEA} k_G} + \frac{1}{E k_L} \tag{19}$$

where N_{CO_2} is the CO_2 mass transferred through the gas-liquid interface, K_L is the overall mass transfer coefficient, k_G and k_L are the mass transfer coefficients in the gas and liquid phases, respectively, R is the gas constant, T is the temperature, H_{CO_2-MEA} is the Henry constant, E is the enhancement factor, which is defined as the ratio of the absorption rate with and without chemical reaction (Sebastia-Saez et al., 2015), and $C^*_{CO_2}$ and C_{CO_2} are the CO_2 concentrations on the surface of the liquid and in the liquid bulk flow, respectively. In particular, H_{CO_2-MEA}, E and $C^*_{CO_2}$ have been adequately illustrated in many works (Borhani et al., 2018; Lu et al., 2019; Pham et al., 2015), so that these factors are expressed in Table 1 along with some other parameters.

Since the CO_2 mass transfer resistance between the gas and liquid is dominated by the liquid side, the CO_2 mass transfer resistance in the gas side is neglected. Therefore, Eq. (19) may be simplified as the following equation:

$$\frac{1}{K_L} = \frac{1}{E k_L} \tag{20}$$

According to the film theory expression, the mass transfer coefficient is given as follows:

$$k_L = \frac{D_{L,CO_2}}{\delta} \tag{21}$$

where D_{L,CO_2} is the diffusivity of the CO_2 in the liquid phase, which could be calculated

by the N_2O analogy method (Liu et al., 2006) and given in Table 1, and δ is the diffusion layer thickness for the mass transfer.

Guo et al. (1997) and Munjal et al. (1989) proposed the correlations for predicting the film thickness for the RPBs, which are shown in Eq. (22) and (23), respectively,

$$\delta = 4.20 \times 10^8 \frac{Q_L}{2\pi r h} \frac{\nu_L}{\omega^2 r} \tag{22}$$

$$\delta = \left(3\left(\frac{Q_L}{2\pi r}\right)\frac{\nu_L}{r\omega^2}\right)^{\frac{1}{3}} \tag{23}$$

where r is the radial distance, ν_L is the kinematic viscosity, and ω is the rotational speed.

For the operating condition in the simulations, the enhancement factor (E) is approximately equal to the Hatta number (Ha) when the reaction is in the fast reaction regime ($5 \leq Ha \ll E_i$) due to the high MEA concentration or the small CO_2 partial pressure given by Eq. (T-7) (Jiru and Eimer, 2013; Ying and Eimer, 2013). As a result, $K_L = Ek_L \approx Hak_L = \sqrt{\frac{k_2 D_{L,CO_2} C_{L,MEA}}{(k_L)^2}} k_L = \sqrt{k_2 D_{L,CO_2} C_{L,MEA}}$, which means that the overall mass transfer rate is almost independent of the film layer thickness. In addition, this conclusion is consistent with that drawn by Lu et al. (2019). Therefore, either of these equations could be utilized in this paper and Eq. (22) is selected in this paper since this equation is derived from the wire mesh (Guo et al., 1997), which is the experimental packing material used in the reference paper (Kolawole, 2019).

2.5 Chemical reaction rate

The CO_2-MEA absorption system can be expressed by the zwitterion mechanism (Danckwerts, 1979), and the overall reaction between CO_2 and MEA is described as follows (Borhani et al., 2018):

$$2\mathrm{MEA} + \mathrm{CO_2} \rightleftharpoons \mathrm{MEACOO^-} + \mathrm{MEAH^+} \tag{24}$$

The above reaction could be separated into two-step reactions. According to the zwitterion mechanism, an intermediate product - the zwitterion ion ($MEAH^+COO^-$) is generated in the CO_2-MEA absorption process (Ebadi Amooghin et al., 2018). Then,

376 **Table 1** Some of the correlations utilized in the current study.

Equation name	Equations	Eq. No.	Reference
Diffusivity of the MEA	$D_{L,MEA} = \exp\left(-13.275 - \frac{2198.3}{T} - 0.078142 C_{L,MEA}\right)$	T-1	(Snijder et al., 1993)
Diffusivity of CO_2 in the MEA solution	$D_{L,CO_2} = D_{L,N_2O} \frac{D_{w,CO_2}}{D_{w,N_2O}}$	T-2	(Liu et al., 2006)
	$D_{w,CO_2} = 2.35 \times 10^{-6} \exp\left(-\frac{2119}{T}\right)$	T-3	
	$D_{w,N_2O} = 5.07 \times 10^{-6} \exp\left(-\frac{2371}{T}\right)$	T-4	
	$D_{L,N_2O} = 5.07 + 0.865 C_{MEA} + 0.278 C_{MEA}^2 \exp\left(-\frac{2371 - 93.4 C_{MEA}}{T}\right)$	T-5	
Enhancement factor	$E = 1 + \left((E_i - 1)^{-1.35} + (E_1 - 1)^{-1.35}\right)^{-\frac{1}{1.35}}$	T-6	(Wellek et al., 1978)
	$E_i = 1 + \frac{D_{L,MEA} C_{L,MEA}}{2 D_{L,CO_2} C_{L,CO_2}}$	T-7	(Sebastia-Saez et al., 2015)
	$E_1 = \frac{Ha}{\tanh(Ha)}$	T-8	
	$Ha = \sqrt{\frac{k_2 D_{L,CO_2} C_{L,MEA}}{(k_L)^2}}$	T-9	
CO_2 saturation concentration	$C_{L,CO_2}^* = M_{CO_2} \frac{P_{CO_2}}{H_{CO_2-L}}$	T-10	(Penttilä et al., 2011)
Henry constant of the CO_2	$H_{CO_2-L} = H_{N_2O-L} \left(\frac{H_{CO_2-H_2O}}{H_{N_2O-H_2O}}\right)$	T-11	(Penttilä et al., 2011)

	$H_{CO_2-H_2O} = \exp\left(145.369 - \frac{8172.355}{T} - 19.303\right)$	T-12	
	$H_{N_2O-H_2O} = \exp\left(158.245 - \frac{9048.596}{T} - 20.86\ln T - 0.00252\right)$	T-13	
	$H_{N_2O-MEA} = \exp\left(-9172.5 + \frac{39.598}{T}\right)$	T-14	
	$H_{N_2O-L} = H_{N_2O-H_2O}C_{L,H_2O} + H_{N_2O-MEA}C_{L,MEA} + 3524641.533(C_{L,H_2O}C_{L,MEA})^2\left(1 - \frac{T}{324.718}\right)\exp(-13.219C_{L,MEA})$	T-15	
Viscosity of the MEA solution	$\mu_{0.3} = 0.3083 - 0.00262T + 7.4882\times10^{-6}T^2 - 7.17293\times10^{9}T^3$ $\mu_{0.9} = 4.37711 - 0.03776T + 1.08945\times10^{-4}T^2 - 1.05031\times10^{7}T^3$	T-16	(Amundsen et al., 2009)
Surface tension of the MEA solution	$\sigma_{H_2O} = 0.18548(1 - \frac{T}{647.13})^{(2.717+3.554(\frac{T}{647.13})+2.047(\frac{T}{647.13})^2)}$	T-17	(Vázquez et al., 1997)
	$\sigma_{MEA} = 0.09945(1 - \frac{T}{614.45})^{(1.067)}$	T-18	
	$\sigma_L = \sigma_{MEA} + \frac{2.129(1-y_{MEA})}{(1+(2.129-(1-y_{MEA})))(\sigma_{H_2O}-\sigma_{MEA})}$	T-19	

377

this zwitterion transfers into carbamate ($MEACOO^-$) via deprotonation by a base (MEA) (Moftakhari Sharifzadeh et al., 2016), and the two-step reactions are as follows:

$$MEA + CO_2 \rightleftharpoons MEAH^+COO^- \quad (25)$$

$$MEAH^+COO^- + MEA \rightarrow MEACOO^- + MEAH^+ \quad (26)$$

Reaction (25) has a finite reaction rate and could be performed in Ansys Fluent through source term UDFs. Reaction (25) (i.e. carbamate formation) is the controlling step and presents the whole reaction kinetics (Sebastia-Saez et al., 2014; Sebastia-Saez et al., 2015). It can be regarded as a second-order irreversible reaction, and the reaction rate is expressed as follows (Luo et al., 2012):

$$r_{CO_2} = -k_2[MEA][CO_2] \quad (27)$$

where k_2 is the reaction rate constant. Different k_2 equations have been proposed for the CO_2-MEA absorption system based on various experimental conditions (Hikita et al., 1977; Luo et al., 2015; Versteeg and van Swaaij, 1988; Ying and Eimer, 2013).

Among them, the reaction rate reported by Versteeg et al. (1996) has been validated by Ying and Eimer (2013) and used in many studies (Dashliborun et al., 2019; Ying and Eimer, 2013), which is given as follows:

$$k_2 = 4.4 \times 10^{11} \exp\left(-\frac{5400}{T}\right) \quad (28)$$

2.6 Heat transfer rate

The amount of the transferred heat between the gas and liquid phases is a function of the temperature difference and the interfacial area:

$$Q_{h,GL} = h_{GL}A_{GL}(T_L - T_G) \quad (29)$$

where $Q_{h,GL}$ is the transferred heat between the two phases, and h_{GL} is the heat transfer rate. A commonly used model- the Hughmark model (Hughmark, 1967) was utilized to calculate the heat transfer rate, namely

$$h_{GL} = \frac{\kappa_G Nu_L}{d_p} \quad (30)$$

403 $$Nu_L = \begin{cases} 2.0 + 0.6Re_L^{\frac{1}{2}}Pr_G^{\frac{1}{3}} & 0 \le Re_L < 776.06, 0 \le Pr_G < 250 \\ 2.0 + 0.27Re_L^{0.62}Pr_G^{\frac{1}{3}} & 776.06 \le Re_L, 0 \le Pr_G < 250 \end{cases} \quad (31)$$

404 $$Pr_G = \frac{C_{pG}\mu_G}{\kappa_G} \quad (32)$$

405 where κ_G is the thermal conductivity of the gas phase, Nu_L is the Nusselt number of the
406 liquid phase, Pr_G is the Prandtl number of the gas phase, and C_{pG} is the specific heat. The
407 heat transfer in the RPB is determined by the heat transfer rate, which is reversely proportional
408 to the liquid droplet diameter according to Eq. (30). The larger the liquid droplet diameter, the
409 lower is the heat transfer rate, which means that more heat could be retained in the liquid phase.
410 As a result, the liquid temperature changes and the CO_2 capture performance is changed.
411 Therefore, the liquid droplet diameter is a critical parameter for the CO_2 absorption, and this
412 parameter in the packing region and outer cavity zone should be carefully modelled. In
413 particular, the diameter of the liquid droplets in the outer cavity zone (Sang et al., 2017b) are
414 shown in Eq. (8) and the diameter in the packing region has been regressed as two
415 correlations based on the same set of the experimental data (Zhang, 1996), namely (Guo et
416 al., 1997; Yi et al., 2009):

417 $$d_{p,P} = 0.7284\left(\frac{\sigma}{\omega^2 r\rho}\right)^{0.5} \quad (33)$$

418 $$d_{p,P} = 12.84\left(\frac{\sigma}{\omega^2 r\rho}\right)^{0.630} u^{0.201} \quad (34)$$

419 where r is the radial coordinate of the packing from the centre, and u is the liquid flow rate
420 per unit area, which is only included in Eq. (34). Since the liquid diameter is influenced by
421 the liquid flow rate u, Eq. (34) could more accurately predict the diameter of the liquid
422 droplets in the packing region. Thus, Eq. (34) has been utilized in this work.

423 **2.7 CFD model setup**

424 Figure 3(a) shows the outside and inside mesh layouts of the 3D pilot-scale RPB model
425 generated by the ANSYS Mesh. In addition to the packing region, the flow characteristics
426 change evidently in the middle of the outer cavity zone and the inner cavity zone, the meshes

in these areas are finer compared with the top and bottom cavity zones. To reduce the number of cells and improve the calculation accuracy (Zhang et al., 2022b), the structured hexahedral grids were generated in the whole RPB except in the inner cavity zone. Various numbers of the grid cell were tested with total cells of 0.16 M, 0.26 M, 0.42 M and 0.76 M in order to obtain a mesh independent solution, which is shown in Figure 3(b). According to Figure 3(b), until a grid of 0.42 M cells, the CO_2 capture rate and liquid outlet temperature reached stable. Finally, the grid of 0.42 M cells, including 0.05 M cells in the packing zone and 0.28 M cells in the outer cavity zone, was applied. The minimum and largest mesh volumes are 1.4×10^{-10} and 3.3×10^{-7} m^{-3}, respectively, and the average skewness and element quality are 0.11 and 0.85, respectively. It should be noted that the mesh number used in this study is adequate only for this case study. A solid mesh study may be required for other applications.

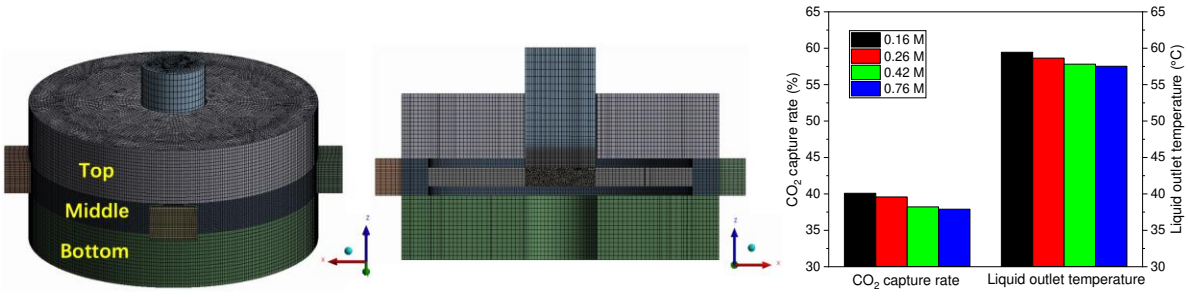

(a) (b)

Figure 3. (a) Schematic of the mesh in the 3D model and (b) predicted CO_2 capture rate and liquid outlet temperature using different grids.

The 3D transient simulations have been performed using the ANSYS Fluent 2021 R1 in a double precision mode based on the High Performance Computing cluster in the University of Sheffield. Various UDFs have been developed for defining the properties of the MEA solution, implementing the extra forces in the momentum equations, and calculating the transferred CO_2 in the mass equations, etc. The Phase Coupled SIMPLE method was applied, and the pressure equations were discretized by the second-order scheme. The pressure-based method and the absolute velocity formulation have been utilized. The time step was set as 5×10^{-4} s, and a maximum of 35 iterations was employed per time step, and the convergence tolerance was

449 1×10^{-5}. The simulation case can be assumed to be the pseudo steady state when the CO_2
450 concentration at the gas outlet and the liquid outlet temperature were reduced to within 1% in
451 ten seconds, and the governing equations' residuals were less than 5×10^{-5}.

452 For the RPB model, the realizable k-ε turbulence model is more suitable for implementation in
453 the RPB than the standard k−ε model, and the reasons are illustrated in our previous paper
454 (Zhang et al., 2022a). In addition, this turbulence model has been frequently used for the fluid
455 flow simulations in RPBs (Wang et al., 2020; Wu et al., 2018; Yang et al., 2010), thus, this
456 model has been employed in this study.

457 The properties of the gas and liquid phases are shown in (Xie, 2019). The gas phase consists
458 of CO_2 and air, and the liquid phase is composed of CO_2, MEA ($HOC_2H_4NH_2$), MEAH+
459 ($HOC_2H_4NH_3^+$), MEACOO$^-$ ($HOC_2H_4NHCOO^-$) and water. The correlations of the surface
460 tension and viscosity for the MEA solution are present in Table 1 (Amundsen et al., 2009;
461 Vázquez et al., 1997). In addition, the liquid density, thermal conductivity and specific heat of
462 the two phases are evaluated by the mixing law based on every species in each phase. The
463 operating conditions are shown in Table 2.

464 **Table 2.** The operational conditions of the experiments (Kolawole, 2019).

MEA concentration (wt%)	Rotational speed (rpm)	Gas flow rate (kg/h)	L/G mass ratio
30, 50, 70	600, 850, 1150	42	1.3-3.5

465 In the experiment conducted by Kolawole (2019), all MEA solutions were preloaded to 0.1 mol
466 CO_2/mol MEA before the MEA solution was fed into the RPB. The same MEA loading is
467 employed in the CFD model. The gas flow rate is fixed at 42 m^3/h with a temperature of 40 °C
468 according to the experimental settings and the gas outlet boundary is set as the pressure-outlet
469 with a zero gauge pressure. In terms of the reverse flow at the gas outlet boundary, the CO_2
470 fraction on the inner packing surface is used as the CO_2 fraction in the gas outlet, which has
471 been performed iteratively. In addition, different L/G mass ratios, e.g. L/G = 2.7, 3.1, 3.5 for
472 30% MEA, are tested in the model. Accordingly, the liquid inlet velocity ranges from 0.20 to
473 0.54 m/s with a temperature fixed at 40 °C and the liquid disappears after entering the liquid

elimination zone. The gravity force is set as 9.8 m/s^2 and in the -Y direction. The rotating speeds employed in the experiment, including 600, 850 and 1150 rpm are used in the simulations. The sliding model has been performed to achieve the motion of the packing. The wall boundaries have been set as no slip and adiabatic.

3. Results and discussion

In order to validate the CFD model developed, 27 simulation cases have been compared with various experimental cases, and all the major variables have been critically analyzed. After that, the effects of various operational parameters on the mass transfer process have been investigated. In addition, the ratio of the CO_2 captured in the outer cavity zone to that in the full-scale RPB has been investigated.

3.1 Validation and the distribution of variables

For validating the developed 3D RPB model, the obtained CO_2 mole fraction in the gas outlet and the liquid temperature at the liquid outlet, which could reflect the mass and heat transfer performance, are compared with the experimental results in the Kolawole thesis (Kolawole, 2019). The full operating conditions are listed in Table 2. Although the flow dynamics may be compared via the liquid holdup, unfortunately, this parameter has not been measured in the experimental investigation.

Figure 4 presented a comparison of the CO_2 fractions in the gas outlet and the liquid outlet temperatures obtained from the experiments and simulations under various operating conditions, including the MEA concentration, rotational speed and the L/G mass ratio. From Figure 4(a), it is observed that all relative deviations of the CO_2 mole fraction are within 15%. And the CO_2 fraction for the 50% MEA solution has a better agreement with the experimental data, whose relative deviations are less than 6%. According to Figure 4(b), most of the relative deviations of the liquid outlet temperature are less than 10%. Only a few points for the 70% MEA solution with a lower rotational speed are larger than 10%. The difference between the simulations and experimental results may mainly result from the difficulties and uncertainties in measuring the variables since the experiments have been conducted in a relatively small

reactor (Lu et al., 2019). In addition, the employed empirical correlations may not be suitable for this RPB model since these correlations were derived from different RPB sizes, operating conditions, etc. Also, the phase properties may not be able to be accurately evaluated as the temperature and CO_2 loading increase. Furthermore, the employed mesh grid with only 0.42 M cells could be a possible reason for the errors between the simulations and experiment results. It can be found that the average absolute relative deviations in the CO_2 fraction and liquid outlet temperature are smaller than 7% and 6%, respectively, thus indicating that the effective interfacial area, mass and heat transfer models could accurately describe the thermodynamics and mass transfer processes within the RPB. Furthermore, the same sub-models, such as the hydrodynamics, including the interfacial, drag, capillary pressure and mechanical dispersion force models, have been verified in our previous paper (Zhang et al., 2022a) using a smaller RPB model. Therefore, it can be concluded that the developed 3D RPB model gives a good match to the experimental results, and it can be employed to investigate the CO_2 capture process within this RPB. It should be noted, although the overall CFD results agree with the experimental data for this RPB, further validation may be required when applying the sub-models to other RPBs, in particular when different packings are employed.

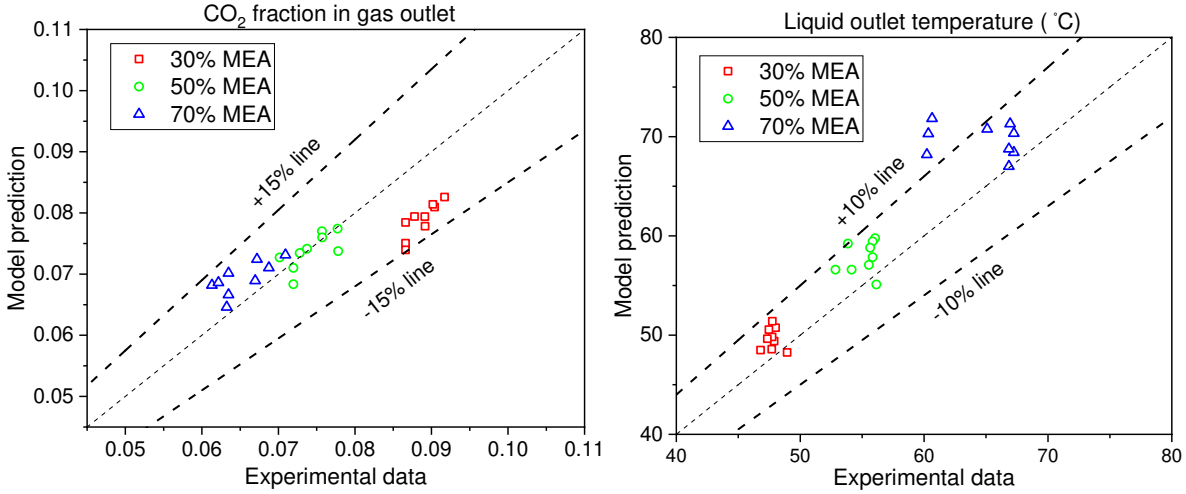

Figure 4. Comparison of the (a) CO_2 mole fraction in the gas outlet; (b) liquid outlet temperature (Kolawole, 2019).

In addition, the distributions of some important variables are presented in order to analyze the

hydrodynamics, thermodynamics, and reaction-enhancement mass transfer within the RPB. Figure 5 presents the predicted variables for the 30% and 70% MEA solutions. Also, the cases are performed with the rotational speed being 850 rpm and the L/G ratios being 3.1 and 1.5 for 30% and 70% MEA solutions, respectively. Since the vectors of the gas and liquid velocities are similar for the 30% and 70% MEA solutions, only the vectors for the 30% MEA solution in half of the RPB cut from the central plane is presented in Figures 5(a) and 5(b) in order to observe them clearly. Figure 5(a) shows that the liquid flows tangentially followed the rotational bed due to the porous resistance and its velocity gradually increases on the way outwards through the packing. Near the outer packing surface, the liquid velocity reaches a maximum and then the liquid velocity suddenly reduces in the outer cavity zone due to the interfacial force between the gas and liquid phases. In addition, the liquid also rotates with a small velocity in the bottom outer cavity zone. From Figure 5(b), it is observed that the gas phase that radially flows from the gas inlet, begins to rotate after entering the outer cavity zone due to the effect of the rotational packing. Its motion is in rapid synchronization with the rotating packing in the outer packing zone and it reacts with the MEA solution when passing through the packing region. It is worth mentioning that although the vectors of the phase velocity in Figures 5(a) and 5(b) are very similar, the radial flow directions of the gas and liquid phases are opposite.

According to Figure 5(c), it is observed that the liquid holdup gradually reduces along the radial direction in the packing zone and this is due to the increasing flow space and the increasing liquid radial velocity due to the centrifugal force, which also can be seen in Figure 6(a). Although the liquid holdup data is not available in the Kolawole's thesis, this phenomenon has been accurately predicted by other simulation and experimental investigators (Burns et al., 2000; Lu et al., 2018). After flowing out from the packing region, the liquid radial velocity suddenly increases without the restriction of the porous resistance, thus causing the liquid fraction to become quite small in the outer cavity zone. Subsequently, the liquid droplets collide on the casing wall and flow downwards under the influence of the gravitational force. Thus, the liquid with a higher volume fraction may be observed on the casing wall surface. Also, it

549 can be found that the liquid holdup for the 30% MEA solution is clearly larger than that for the
550 70% MEA solutions as the ratio of the liquid flow rate for 30% to 70% MEA is 2.1. However,
551 the ratio of the liquid holdup in the packing regions is about 1.6, which is smaller than the ratio
552 of the liquid flow rate of 2.1. The first reason is that the liquid viscosity for the 70% MEA is
553 larger, which means that the 70% MEA solution is more likely to adhere to the wire mesh
554 surface (Xie et al., 2019). Furthermore, the liquid radial velocity increases and the liquid
555 residence time reduces when more of the liquid phase enters the packing zone, which allows
556 the 30% MEA solution to faster escape into the packing. These factors lead to a higher liquid
557 holdup for the 30% MEA solution and thus the ratio of the liquid holdup is not exactly equal
558 to the ratio of the liquid flow rate. As a result, the effective interfacial area for the 30% MEA
559 solution is larger, see Figure 5(c), since more liquid is attached to the wire mesh packing surface,
560 or it is split into numerous small droplets in the packing zone (Liu et al., 2019; Yang et al.,
561 2015a). This means that the contact area between the gas and liquid phases is larger, thus
562 indicating that the 30% MEA solution has more chance to interact with the CO_2.

563 Although the liquid holdup and contact area are larger for the 30% MEA solution resulting
564 from the larger liquid flow rate, the CO_2 fraction in the gas outlet is higher by comparing the
565 two illustrations in Figure 5(e). This is because the CO_2 capture performance is not only related
566 to the liquid holdup and contact area, but also it is affected by some other parameters, such as
567 the MEA concentration, liquid temperature and residence time. Clearly the MEA concentration
568 is the dominant factor in determining the CO_2 capture process. For the CO_2-MEA absorption
569 system, the heat will be released when the CO_2 is captured in the MEA solution, thus leading
570 to an increasing liquid temperature. Simultaneously, some heat is taken away by the opposing
571 gas flow via the heat transfer and the rest of the heat remains in the liquid phase. This could be
572 the reason why the liquid temperature for the 70% MEA solution is higher than that for the 30%
573 MEA solution, see Figure 5(f), because more active MEA participates in the reaction and
574 releases more heat to the already smaller flow rate of the liquid phase (Vaewhongs et al., 2020).
575 This phenomenon is more clearer in the top and bottom outer cavity zones, where the liquid
576 fraction is quite low and the liquid temperature could be even up to 89 °C. In return, the

chemical reaction is faster when the phase temperature is higher. In addition, the phase temperature could also influence the physical properties, including the viscosity and density, which further has an impact on the flow dynamics, such as the liquid holdup and residence time. Thus, this indicates that the liquid holdup, CO_2 capture rate, and liquid temperature could affect each other in this system. The predicted variables can be made accurate and stable only when all the parameters related to the flow dynamics, mass and heat transfer are set properly and these processes reach a balance within the whole RPB.

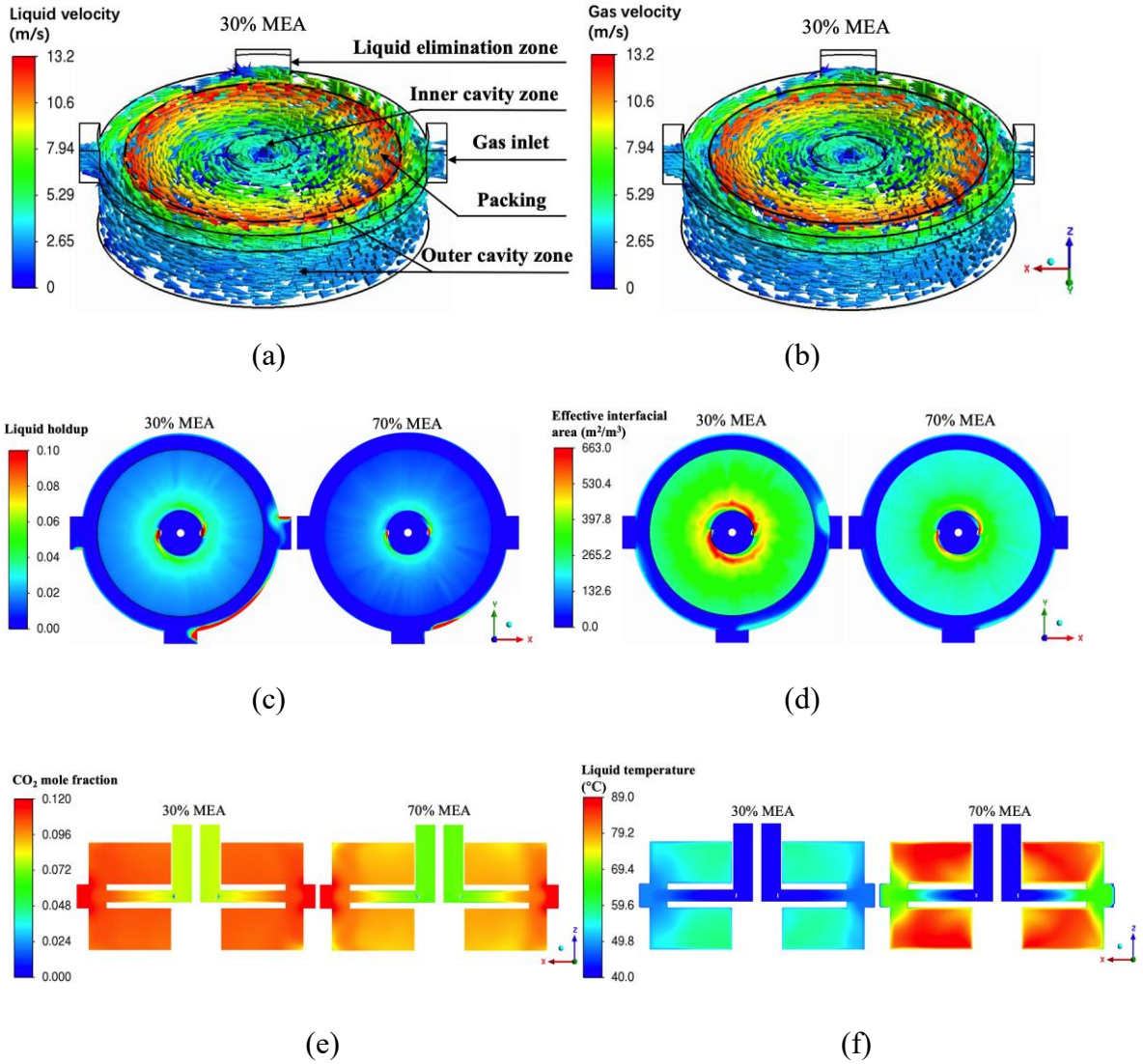

Figure 5. Vectors of the (a) liquid velocity; (b) gas velocity; contours of the (c) liquid holdup; (d) effective interfacial area on the planes z = 0.01; (e) CO_2 fraction in the gas phase; and (f) liquid temperature on the planes y=0 for 30% and 70 % MEA.

3.2 Mass transfer in different zones in the RPB

As we know, the CO_2 absorption within a RPB mainly occurs in two zones: packing and outer cavity zones. Based on the newly developed 3D full-scale RPB model, where the CO_2 capture process in the packing and outer cavity zones is separately analyzed by using the CFD method.

Taking the 50% MEA solution with a L/G ratio of 2.1 in Section 3.1 as an example, Figures 6(a), 6(b) and 6(c) show the circumferentially averaged liquid holdup and effective interfacial area (per unit, m^2/m^3), liquid velocity, as well as the CO_2 mole fraction in the gas phase and the liquid temperature along the radial direction, respectively. For $r_i \leq r \leq r_o$, these parameters are only circumferentially averaged in the packing region rather than including the top and bottom cavity zones. When flowing into the inner packing zone, with a radial velocity only, the liquid violently collides with the rotational packing and it is quickly dispersed, thus generating numerous very small tiny droplets, or forming thin films on the wire mesh surface. Due to the small flow space in the inner periphery of the packing, a large effective interfacial area could be observed in Figure 6(a), which is defined as the "end-effect zone" - an area where excellent micromixing occurs due to the strong interaction and liquid dispersion (Cortes Garcia et al., 2017; Esmaeili et al., 2022). Although the phase surface renewal is fast and the effective interfacial area is large in the end-effect zone, a sharp decrease in the CO_2 fraction is not observed in Figure 6(c) due to the small local CO_2 fraction in the gas phase flow and the low liquid temperature.

Soon after entering the bulk of the packing zone, the liquid starts to synchronize with the rotating packing, and its tangential velocity almost coincides with the packing rotational velocity in Figure 6(b). Consequently, the liquid dispersion is relatively weak, thus the effective interfacial area decreases along with the radial position in Figure 6(a) (Zhang et al., 2017). Since smaller droplets and thinner film are formed in this region, the liquid radial velocity gradually decreases due to the larger interfacial and drag forces, which is shown in Figure 6(b). In this packing region, most of the CO_2 is captured and a large amount of heat is released, and this is due to the large interfacial surface area and the enhanced surface renewal of the phases

(Wang et al., 2021). Therefore, the CO_2 fraction in the gas phase reduces and the liquid temperature increases on their way through the packing as shown in Figure 6(c).

After flowing out from the outer edge of the packing, the liquid droplets with large velocity pass through the cavity space, causing a sudden decrease in the effective interfacial area and liquid holdup in Figure 6(a). Without the interaction with the packing, the liquid flow direction is almost unchanged in the outer cavity space, thus causing the liquid radial velocity component to increase and the tangential velocity component to decrease as shown in Figure 6(b). As a result, the difference between the gas and liquid radial velocity increases, which leads to an increase in the interfacial force between the two phases and a decrease in the total liquid velocity. In addition, an increase in the liquid temperature can be observed in Figure 6(c) due to the high liquid temperature in the top and bottom regions of the outer cavity zone (see Figure 5(f)). Then the liquid droplets collide on the inner casing wall, generating the liquid film and a large number of splashing droplets (Sang et al., 2017b). These phenomena have been modelled well with a steep increase in the liquid holdup and effective interfacial area, see Figure 6(a). Figure 6(c) shows that the magnitude of the decreased CO_2 fraction is small in the outer cavity zone due to the low average effective interfacial area.

In general, the outer cavity zone's volume is much larger than the packing region. For instance, the volume of the outer cavity zone to the packing region is about 11 for the present employed RPB model. However, most of the CO_2 is captured in the packing region instead of the outer cavity zone, which means that the larger the volume of the packing occupied in the fixed full-scale RPB, the more effective is the CO_2 absorption.

Based on the validation cases under various operating conditions shown in Figure 4, it is found that the outer cavity zone takes up 25%~40% of the total effective interfacial area and the effect of the outer cavity zone on the mass transfer could range from 28% to 42% for this case study. From the wide range of the contribution of the mass transfer and effective interfacial area in the outer cavity zone, it is known that the CO_2 capture process in the packing and outer cavity zones are quite different under various operating conditions. With the aim of providing some

new, useful and important suggestions for RPB design and scaling up, the contribution of the CO_2 removal and effective interfacial area in different zones has been investigated, which is presented in the following section.

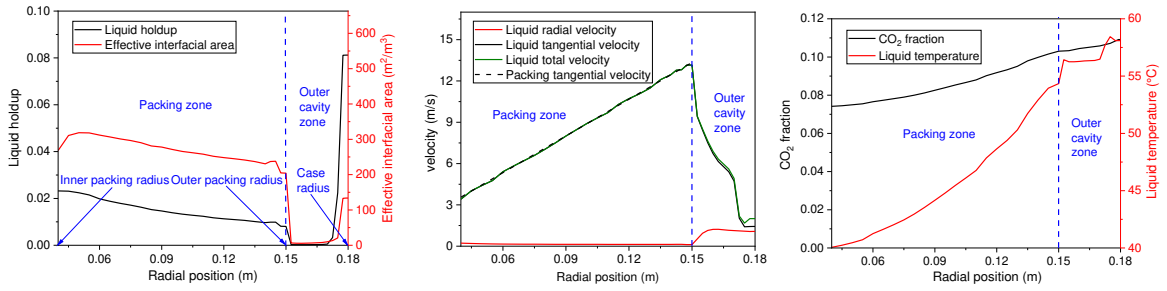

(a) (b) (c)

Figure 6. The circumferentially averaged (a) liquid holdup and effective interfacial area; (b) liquid and rotating packing velocities and (c) CO_2 mole fraction in the gas phase and liquid temperature along the radial direction.

3.3 Effect of the operating parameters

Among the three MEA concentrations investigated, the relative deviation of the CO_2 fraction in the gas outlet for the 50% MEA solution is small, as discussed in Section 3.1. Thus, the 50% MEA solution is selected as the baseline case for discussion, and its operating conditions are listed in Table 3.

Table 3. The operational conditions for the baseline case.

MEA concentration (%)	L/G ratio	Rotational speed (rpm)	Liquid inlet temperature (°C)	Gas flow rate (kg/s)
50	2.1	850	40	42

For evaluating the CO_2 absorption performance in the full-scale RPB, the overall volumetric mass transfer coefficient ($K_L a_e$), a parameter that may determine the rate at which a gaseous compound (CO_2) can transfer from the gas phase to the MEA solution, is introduced along with the liquid temperature at the liquid outlet. The equation for $K_L a_e$ is shown in Eq. (35). $K_L a_e$becomes larger when the CO_2 fraction in the gas outlet ($y_{CO_2 out}$) is lower, indicating a better CO_2 capture performance.

$$K_L a_e = \frac{Q_G}{\pi(r_o^2 - r_i^2)Z} \ln\left(\frac{y_{CO_2 in}}{y_{CO_2 out}}\right) \quad (35)$$

664 The ratios of the captured CO_2 (r_c) and the effective interfacial area (r_e) in the outer cavity zone
665 to those in the whole RPB are examined in order to analyze the mass transfer in different zones.
666 The expression for r_c and r_e are given as follows:

667 $$r_c = \frac{y_{i,CO_2} - y_{op,CO_2}}{y_{i,CO_2} - y_{o,CO_2}} \tag{36}$$

668 $$r_e = \frac{\int_O a_e dV}{\int_P a_e dV + \int_O a_e dV} \tag{37}$$

669 **(i) Effect of the MEA concentration**

670 It is known that the CO_2 capture efficiency increases when using the solution with a higher
671 MEA concentration. In terms of the flow dynamics, the liquid phase can lead to early flooding
672 or abnormal distribution in the packing of a CPB due to its large viscosity. However, one of the
673 advantages of applying the RPB is that a higher MEA concentration solution with larger
674 viscosity can fluently pass through the packing due to the higher gravitational environment.

675 Figure 7(a) illustrates the influence of the MEA concentration on the CO_2 absorption and
676 thermodynamics in the RPB in terms of $K_L a_e$and liquid temperature at the liquid outlet. In this
677 case study, the MEA concentration varies from 30 to 70% while keeping all the other operating
678 conditions consistent with the base case. It can be observed that the magnitude of the increased
679 $K_L a_e$ and liquid outlet temperature significantly becomes larger when using a higher MEA
680 concentration solution since the increased active MEA available in the solution could remove
681 more CO_2 from the gas phase and more reaction heat would be generated at the same time
682 (Qing et al., 2011). Although the solution with a higher MEA concentration favors for the CO_2
683 absorption, the greater trend for corrosion, degradation and foaming should be carefully
684 considered before the PCC industrial application.

685 Figure 7(b) illustrates the ratios of the CO_2 capture and effective interfacial area in the outer
686 cavity zone to the whole RPB under the same operating conditions as Figure 7(a). On one hand,
687 the effective interfacial area mainly depends on the liquid flow rate and rotational speed. On
688 other hand, the increasing temperature in Figure 7(a) affects the phase properties, such as the
689 density and viscosity. As a results, the r_e changes only slightly in Figure 7(b).

On considering Figure 7(b), the liquid temperature approximately reaches the maximum after entering the outer cavity zone, which means that the average liquid temperature is relatively high in the outer cavity zone compared with that in the packing zone. The higher liquid temperature benefits the reaction rate. Therefore, the proportion of the CO_2 removed in the outer cavity zone (r_c) increases as the MEA concentration increases. From the above analysis, it is indicated that the higher MEA concentration could enhance the CO_2 capture in the full RPB, and more proportions of CO_2 are captured in the outer cavity zone.

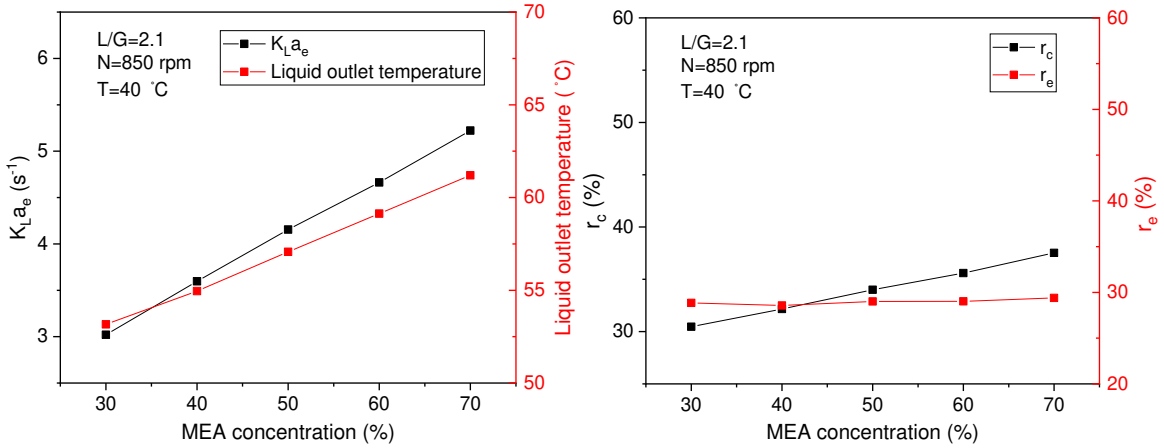

Figure 7. The effect of the MEA concentration on (a) $K_L a_e$ and liquid outlet temperature and (b) ratio of the contribution of CO_2 capture and effective interfacial area in the outer cavity zone.

(ii) Effect of the liquid flow rate

For post-combustion capture using the CPB, it is reported that the liquid outlet temperature and CO_2 capture level increase when the L/G ratio increases due to the larger amount of free amine molecules and the higher effective interfacial area (Sønderby et al., 2013). However, a reduced liquid outlet temperature is observed in the RPB from the experimental work (Kolawole, 2019). Therefore, it is worth exploring the difference in the CO_2 capture processes under various L/G ratios within the CPB and RPB.

Figure 8(a) presents the predicted impact of the L/G ratio on $K_L a_e$ and liquid outlet temperature with the L/G ratio ranging from 1.5 to 2.7 while keeping the gas flow rate unchanged. As the L/G ratio increases, more CO_2 is captured resulting from the larger amount of free amine

711 molecules and also the mass transfer resistance is reduced due to the enhanced gas-liquid
712 mixing (Luo et al., 2021) and liquid film refreshing. In addition, the increasing L/G ratio leads
713 to a higher effective interfacial area. These factors increase $K_L a_e$, but this increase tends to
714 slow down as L/G increases. Although increasing the number of tiny droplets that could be
715 generated, the increase in the effective interfacial area is limited at the higher range of the liquid
716 flow rate (Wu et al., 2017). Similarly, although more heat is generated as the L/G ratio increases,
717 the heat generation is not high enough to increase the liquid temperature due to the large
718 sensible heat of the liquid phase. In addition, this may explain the decreasing liquid outlet
719 temperature in Figure 8(a), which is consistent with the Kolawole's experimental results
720 (Kolawole, 2019). This is different from that typically observed in a CPB because the liquid
721 flow rate in a CPB is the dominant factor that could significantly increase the interfacial area
722 leading to the significantly increased mass transfer and heat generation. From the above
723 analysis, the increased liquid flow rate, effective interfacial area and the decreased liquid
724 temperature together cause $K_L a_e$ to increase more slowly (Kuntz and Aroonwilas, 2009).

725 Figure 8(b) shows the ratios of the CO_2 capture and effective interfacial area in the outer cavity
726 zone to the whole RPB for L/G ratio from 1.5 to 2.1. The r_c and r_e slightly change with
727 changing L/G ratios, but it is noted that a critical point is observed in Figure 8(b). As the L/G
728 ratio increases from 1.5 to 2.1, more liquid concentrates in the outer cavity zone and the
729 temperature in this zone is relatively higher. As a result, both r_c and r_e increase. While the L/G
730 ratio continues to increase, the liquid turbulence is dominant in the packing region and the
731 liquid temperature continues to decrease in the outer cavity zone. As a result, the CO_2 that is
732 captured in the packing increases, thus leading to a reduced value of r_c and r_e.

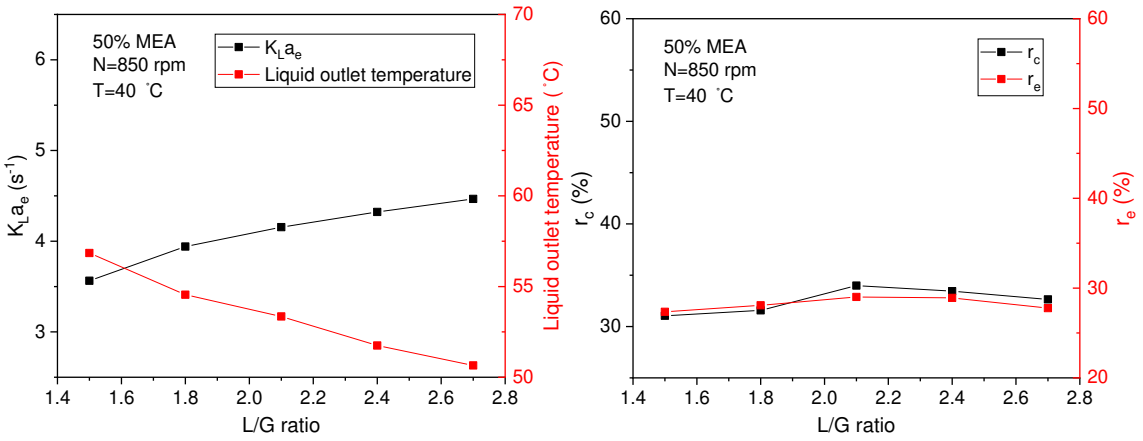

(a) (b)

Figure 8. The effect of the L/G ratio on (a) $K_L a_e$ and liquid outlet temperature and (b) ratios of the contribution of CO_2 capture and effective interfacial area in the outer cavity zone.

(iii) Effect of the rotational speed

In our previous investigation (Zhang et al., 2022a), it was reported that the rotational speed has a considerable impact on the liquid holdup and liquid distribution, thus it will further affect the CO_2 capture in the RPB absorber. In addition, the rotational speed could directly affect the effective interfacial area and the reaction time between the liquid and gas phases. Thus, it is a key parameter for the PCC in a RPB.

Figure 9(a) presents the impact of the rotational speed on the $K_L a_e$, the liquid outlet temperature of the entire RPB and the liquid temperature at the outer packing boundary. Figure 9(b) illustrates the ratios of the CO_2 captured and effective interfacial area in the outer cavity zone to the whole RPB under various rotational speeds. As the rotational speed increases, the liquid holdup in the packing region reduces due to the stronger centrifugal force. However, more tiny liquid droplets are formed among the packing region, which results in an improved effective interfacial area (Zhang et al., 2022a), although the magnitude of the improvement is very limited. On the other hand, the liquid fraction in the outer cavity zone becomes larger because the liquid accumulation in the outer cavity zone relies on the gravitational force to remove out of the RPB. In addition, more liquid is more likely to attach and cover the casing wall when it flows out from the packing with a higher rotational speed, which leads to a significant increase in the effective interfacial area in the outer cavity zone. Thus, the r_e in

Figure 9(b) gradually increases as the rotational speed increases. And the increasing effective interfacial area in both the packing and outer cavity zones makes the $K_L a_e$ increase in Figure 9(a).

From Figure 9(a), the liquid temperature flowing out the packing region (blue line) increases with the rotational speed increasing and it is always lower than the liquid outlet temperature (red line). However, the liquid outlet temperature reduces when the rotational speed increases from 600 to 850 rpm. The possible reason is that in the outer cavity zone, the liquid fraction increases more significantly compared with the increase in the effective interfacial area when the rotational speed increases from 600 to 850 rpm. And the reaction heat generated in this zone at 850 rpm cannot significantly increase the temperature of the liquid with a large fraction. Therefore, the liquid outlet temperature at 850 rpm slightly reduces from the value at 600 rpm.

In addition, r_e increases as the rotational speed increases, thus, r_c is expected to increase accordingly. However, r_c reduces in the range of 300 to 850 rpm as observed in Figure 9(b). The possible reason is that the micromixing performance in the packing region improves significantly at the lower rotational speed (Ouyang et al., 2019). As a result, the packing region captures more CO_2 compared with the outer cavity zone when the rotational speed increases from 300 to 850 rpm. Overall, the $K_L a_e$ and r_e increase with the increase in the rotational speed, and r_c decreases first and then increases.

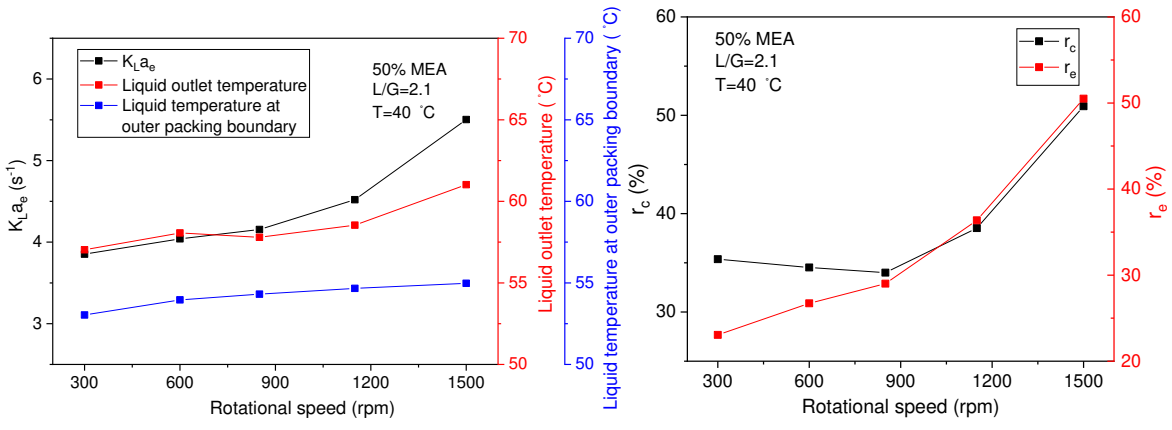

(a) (b)

773 **Figure 9.** The effect of the rotational speed on the (a) $K_L a_e$ and liquid temperatures at liquid
774 outlet and outer packing boundary and (b) ratios of the contribution of CO_2 capture and
775 effective interfacial area in the outer cavity zone.

776 **4. Conclusions**

777 This paper has established a full 3D RPB model using the Eulerian porous medium approach,
778 and the physical and chemical processes occurring in the packing and outer cavity zone of a
779 pilot scale RPB have been modelled. The overall CFD results agree with the experimental data.
780 Nonetheless, further validation may be required when applying the sub-models to other RPBs,
781 in particular when different packings are employed. The main findings of this paper are as
782 follows: (i) a new completed 3D Eulerian porous medium RPB model was established based
783 on a pilot scale RPB model. By using the Eulerian porous medium modelling method, the CO_2
784 absorption performance within a whole RPB could be effectively investigated due to the
785 significantly reduced computational cost; (ii) the force, effective interfacial area, heat transfer,
786 mass transfer models were coupled with the Eulerian RPB model, thus, the hydrodynamics,
787 thermodynamics and mass transfer processes could be thoroughly analyzed; (iii) the effective
788 interfacial area, force and even liquid droplet diameter models were introduced separately for
789 the packing region and the outer cavity zone for accurately predicting the CO_2 capture
790 performance inside the full RPB, and the CO_2 absorption processes in these zones were
791 quantitatively evaluated under various operating conditions by the CFD method for the first
792 time.

793 The predicted simulation results are in good agreement with the experimental data by
794 comparing the CO_2 fraction in the gas outlet and liquid outlet temperature. In addition, the
795 end-effect zone is observed near the inner packing region where a large gas-liquid contact area
796 and strong micromixing occur due to the liquid dispersion and strong interaction between the
797 liquid and packing. However, the amount of the CO_2 transferred between the phases is small
798 in the end-effect zone due to the small local CO_2 fraction in the gas phase and the low liquid
799 temperature.

The outer cavity zone has an effect on the CO_2 capture inside the RPB. The contributions of the outer cavity zone to the effective interfacial area and CO_2 capture are respectively in the ranges of 25%~40% and 28%~42% in the RPB investigated in this paper. However, of course, these values may be different for different designs. Also, the simulation results show that the CO_2 captured in the outer cavity zone becomes more as the MEA concentration increases, however, the MEA concentrations have little effect on the ratio of the effective interfacial area in the outer cavity zone to the whole RPB. The contributions of the outer cavity zone to the effective interfacial area and CO_2 capture change slightly with the L/G ratio increasing. With the increase in the rotational speed, the ratio of the effective interfacial area in the outer cavity zone to the whole RPB increases, however, the ratio of the CO_2 capture in the outer cavity zone to the whole RPB first decreases slightly and then increases significantly.

The RPB model developed in this paper can successfully and effectively predict the CO_2 capture process in the whole RPB, and this demonstrates the substantial potential of the model, with further validation, to be used for process optimization and design of the large-scale RPB for industrial PCC. There are two limitations of the CFD model proposed in this study. The first is that using the porous media approach, the details of the fluid flows are not resolved, and therefore the characteristics of the formation of liquid droplets/films are unable to be revealed. Secondly, the accuracy of the model is highly dependent on the applicability of the sub-models employed and therefore, careful validation of the model should be considered, especially when a very different packing is employed for the RPB.

Acknowledgement

Support from the EPSRC UKCCSRC grant EP/P026214/1 is acknowledged.

Reference

Amundsen, T.G., Øi, L.E., Eimer, D.A., 2009. Density and viscosity of monoethanolamine+water+carbon dioxide from (25 to 80) C. Journal of Chemical & Engineering Data 54, 3096-3100.

Borhani, T.N., Oko, E., Wang, M., 2018. Process modelling and analysis of intensified CO_2 capture using monoethanolamine (MEA) in rotating packed bed absorber. Journal of Cleaner

Production 204, 1124-1142.
Cortes Garcia, G.E., van der Schaaf, J., Kiss, A.A., 2017. A review on process intensification in HiGee distillation. J. Chem. Technol. Biot 92, 1136-1156.
Danckwerts, P., 1979. The reaction of CO_2 with ethanolamines. Chem. Eng. Sci. 34, 443-446.
Dashliborun, A.M., Larachi, F., Taghavi, S.M., 2019. Gas-liquid mass-transfer behavior of packed-bed scrubbers for floating/offshore CO_2 capture. Chem. Eng. J. 377.
Ebadi Amooghin, A., Moftakhari Sharifzadeh, M.M., Zamani Pedram, M., 2018. Rigorous modeling of gas permeation behavior in facilitated transport membranes (FTMs); evaluation of carrier saturation effects and double-reaction mechanism. Greenh. Gases: Sci. Technol 8, 429-443.
Esmaeili, A., Tamuzi, A., Borhani, T.N., Xiang, Y., Shao, L., 2022. Modeling of carbon dioxide absorption by solution of piperazine and methyldiethanolamine in a rotating packed bed. Chem. Eng. Sci. 248.
Fourati, M., Roig, V., Raynal, L., 2013. Liquid dispersion in packed columns: Experiments and numerical modeling. Chem. Eng. Sci. 100, 266-278.
Garba, M.U., 2012. Prediction of ash deposition for biomass combustion and coal/biomass co-combustion. University of Leeds.
Gbadago, D.Q., Oh, H.T., Oh, D.H., Lee, C.H., Oh, M., 2020. CFD simulation of a packed bed industrial absorber with interbed liquid distributors. Int. J. Greenh. Gas Con. 95.
Guo, F., Zheng, C., Guo, K., Feng, Y., Gardner, N.C., 1997. Hydrodynamics and mass transfer in cross-flow rotating packed bed. Chem. Eng. Sci. 52, 3853-3859.
Guo, J., Jiao, W., Qi, G., Yuan, Z., Liu, Y., 2019. Applications of high-gravity technologies in gas purifications: A review. Chin. J. Chem. Eng. 27, 1361-1373.
Guo, K., Zhang, Z., Luo, H., Dang, J., Qian, Z., 2014. An innovative approach of the effective mass transfer area in the rotating packed bed. Ind. Eng. Chem. Res. 53, 4052-4058.
Guo, T.Y., Shi, X., Chu, G.W., Xiang, Y., Wen, L.X., Chen, J.F., 2016. Computational fluid dynamics analysis of the micromixing efficiency in a rotating-packed-bed reactor. Ind. Eng. Chem. Res. 55, 4856-4866.
Hikita, H., Asai, S., Ishikawa, H., Honda, M., 1977. The kinetics of reactions of carbon dioxide with monoethanolamine, diethanolamine and triethanolamine by a rapid mixing method. the chemical Engineering Journal 13, 7-12.
Hughmark, G.A., 1967. Mass and heat transfer from rigid spheres. AlChE J. 13, 1219– 1221.

Iliuta, I., Larachi, F., Fourati, M., Raynal, L., Roig, V., 2014. Flooding limit in countercurrent gas-liquid structured packed beds-Prediction from a linear stability analysis of an Eulerian two-fluid model. Chem. Eng. Sci. 120, 49-58.

Ishii, M., Zuber, N., 1979. Drag coefficient and relative velocity in bubbly, droplet or particulate flows. AlChE J. 25, 843-855.

Jiang, Y., Khadilkar, M., Al-Dahhan, M., Dudukovic, M., 2002. CFD of multiphase flow in packed-bed reactors: I. k-Fluid modeling issues. AlChE J. 48, 701-715.

Jiru, Y., Eimer, D.A., 2013. A study of mass transfer kinetics of carbon dioxide in (monoethanolamine + water) by stirred cell. Energy Procedia 37, 2180-2187.

Khan, M.Z.A., 2017. Causes and consequences of greenhouse effect & its catastrophic problems for Earth. Inter. J. Sustainability Management and Information Technologies 3, 34.

Kim, J., Pham, D.A., Lim, Y.I., 2016. Gas-liquid multiphase computational fluid dynamics (CFD) of amine absorption column with structured-packing for CO_2 capture. Comput. Chem. Eng. 88, 39-49.

Kim, J., Pham, D.A., Lim, Y.I., 2017. Effect of gravity center position on amine absorber with structured packing under offshore operation: Computational fluid dynamics approach. Chem. Eng. Res. Des. 121, 99-112.

Kolawole, T.O., 2019. Intensified post-combustion carbon capture using a pilot scale rotating packed bed and monoethanolamine solutions. Newcastle University.

Kuntz, J., Aroonwilas, A., 2009. Mass-transfer efficiency of a spray column for CO_2 capture by MEA. Energy Procedia 1, 205-209.

Lee, J., Kolawole, T., Attidekou, P., 2017. Carbon capture from a simulated flue gas using a rotating packed bed adsorber and monoethanolamine (MEA). Energy Procedia 114, 1834-1840.

Liu, G.B., Yu, K.T., Yuan, X.G., Liu, C.J., Guo, Q.C., 2006. Simulations of chemical absorption in pilot-scale and industrial-scale packed columns by computational mass transfer. Chem. Eng. Sci. 61, 6511-6529.

Liu, Y.Z., Luo, Y., Chu, G.W., Liu, W., Shao, L., Chen, J.F., 2019. Liquid holdup and wetting efficiency in a rotating trickle-bed reactor. AlChE J. 65.

Lu, X., Xie, P., Ingham, D.B., Ma, L., Pourkashanian, M., 2019. Modelling of CO_2 absorption in a rotating packed bed using an Eulerian porous media approach. Chem. Eng. Sci. 199, 302-318.

Lu, X., Xie, P., Ingham, D.B., Ma, L., Pourkashanian, M., 2018. A porous media model for

892 CFD simulations of gas-liquid two-phase flow in rotating packed beds. Chem. Eng. Sci. 189,
893 123–134
894 Luo, X., Hartono, A., Hussain, S., F. Svendsen, H., 2015. Mass transfer and kinetics of carbon
895 dioxide absorption into loaded aqueous monoethanolamine solutions. Chem. Eng. Sci. 123, 57-
896 69.
897 Luo, X., Hartono, A., Svendsen, H.F., 2012. Comparative kinetics of carbon dioxide absorption
898 in unloaded aqueous monoethanolamine solutions using wetted wall and string of discs
899 columns. Chem. Eng. Sci. 82, 31-43.
900 Luo, X., Wang, M., Lee, J., Hendry, J., 2021. Dynamic modelling based on surface renewal
901 theory, model validation and process analysis of rotating packed bed absorber for carbon
902 capture. Appl. Energy 301.
903 Luo, Y., Luo, J.Z., Chu, G.W., Zhao, Z.Q., Arowo, M., Chen, J.F., 2017. Investigation of
904 effective interfacial area in a rotating packed bed with structured stainless steel wire mesh
905 packing. Chem. Eng. Sci. 170, 347-354.
906 Mardani, A., Mahalegi, H. K. M., 2019. Hydrogen enrichment of methane and syngas for
907 MILD combustion. Int. J. Hydrog. Energy 44, 9423-9437.
908 Moftakhari Sharifzadeh, M.M., Ebadi Amooghin, A., Zamani Pedram, M., Omidkhah, M.,
909 2016. Time-dependent mathematical modeling of binary gas mixture in facilitated transport
910 membranes (FTMs): A real condition for single-reaction mechanism. J. Ind. and Eng. Chem.
911 39, 48-65.
912 Munjal, S., Dudukovć, M.P., Ramachandran, P., 1989. Mass-transfer in rotating packed beds-
913 I. Development of gas-liquid and liquid-solid mass-transfer correlations. Chem. Eng. Sci. 44,
914 2245-2256.
915 Ouyang, Y., Xiang, Y., Gao, X.Y., Zou, H.K., Chu, G.W., Agarwal, R.K., Chen, J.F., 2019.
916 Micromixing efficiency optimization of the premixer of a rotating packed bed by CFD. Chem.
917 Eng. Process. 142.
918 Penttilä, A., Dell'Era, C., Uusi-Kyyny, P., Alopaeus, V., 2011. The Henry's law constant of N_2O
919 and CO_2 in aqueous binary and ternary amine solutions (MEA, DEA, DIPA, MDEA, and AMP).
920 Fluid Phase Equilib. 311, 59-66.
921 Pham, D.A., Lim, Y.I., Jee, H., Ahn, E., Jung, Y., 2015. Porous media Eulerian computational
922 fluid dynamics (CFD) model of amine absorber with structured-packing for CO_2 removal.
923 Chem. Eng. Sci. 132, 259-270.

924 Qing, Z., Yincheng, G., Zhenqi, N., 2011. Experimental studies on removal capacity of carbon
925 dioxide by a packed reactor and a spray column using aqueous ammonia. Energy Procedia 4,
926 519-524.
927 Sang, L., Luo, Y., Chu, G.W., Liu, Y.Z., Liu, X.Z., Chen, J.F., 2017a. Modeling and
928 experimental studies of mass transfer in the cavity zone of a rotating packed bed. Chem. Eng.
929 Sci. 170, 355-364.
930 Sang, L., Luo, Y., Chu, G.W., Zhang, J.P., Xiang, Y., Chen, J.F., 2017b. Liquid flow pattern
931 transition, droplet diameter and size distribution in the cavity zone of a rotating packed bed: A
932 visual study. Chem. Eng. Sci. 158, 429-438.
933 Sang, L., Luo, Y., Chu, G.W., Sun, B.C., Zhang, L.L., Chen, J.F., 2019. A three-zone mass
934 transfer model for a rotating packed bed. AlChE J. 65.
935 Sebastia-Saez, D., Gu, S., Ranganathan, P., 2014. Volume of Fluid modeling of the reactive
936 mass transfer of CO_2 into aqueous amine solutions in structured packed elements at micro-
937 scale. Energy Procedia 63, 1229-1242.
938 Sebastia-Saez, D., Gu, S., Ranganathan, P., Papadikis, K., 2015. Micro-scale CFD modeling of
939 reactive mass transfer in falling liquid films within structured packing materials. Int. J. Greenh.
940 Gas Con. 33, 40-50.
941 Snijder, E.D., te Riele, M.J., Versteeg, G.F., Van Swaaij, W., 1993. Diffusion coefficients of
942 several aqueous alkanolamine solutions. J. Chem. Eng. Data 38, 475-480.
943 Sønderby, T.L., Carlsen, K.B., Fosbøl, P.L., Kiørboe, L.G., von Solms, N., 2013. A new pilot
944 absorber for CO_2 capture from flue gases: Measuring and modelling capture with MEA solution.
945 Int. J. Greenh. Gas Con. 12, 181-192.
946 Vaewhongs, P., Photein, K., Nimchareon, R., Limlertchareonwanit, T., Minakanishtha, K.,
947 Maneeintr, K., Charinpanitkul, T., 2020. Gas-phase mass transfer coefficient of CO_2 in different
948 alkanolamine solutions within packed-bed absorption column. AIP Conf. Proc. 2279, 90001.
949 Vázquez, G., Alvarez, E., Navaza, J.M., Rendo, R., Romero, E., 1997. Surface tension of binary
950 mixtures of water + monoethanolamine and water + 2-amino-2-methyl-1-propanol and tertiary
951 mixtures of these amines with water from 25 C to 50 C. J. Chem. Eng. Data 42, 57-59.
952 Versteeg, G., Van Dijck, L., van Swaaij, W.P.M., 1996. On the kinetics between CO_2 and
953 alkanolamines both in aqueous and non-aqueous solutions. An overview. Chem. Eng. Commun.
954 144, 113-158.
955 Versteeg, G., van Swaaij, W.P.M., 1988. On the kinetics between CO_2 and alkanolamines both

956 in aqueous and non-aqueous solutions-I. Primary and secondary amines. Chem. Eng. Sci. 43,
957 573-585.
958 Wang, J.Q., Ouyang, Y., Li, W.L., Esmaeili, A., Xiang, Y., Chen, J.F., 2020. CFD analysis of
959 gas flow characteristics in a rotating packed bed with randomly arranged spherical packing.
960 Chem. Eng. J. 385.
961 Wang, Y., Li, Y.B., Su, M.J., Chu, G.W., Sun, B.C., Luo, Y., 2021. Liquid droplet dispersion in
962 a rotating packed bed: Experimental and numerical studies. Chem. Eng. Sci., 240
963 Wellek, R., Brunson, R., Law, F., 1978. Enhancement factors for gas-absorption with second-
964 order irreversible chemical reaction. Can. J. Chem. Eng. 56, 181-186.
965 Wu, W., Luo, Y., Chu, G.W., Liu, Y., Zou, H.K., Chen, J.F., 2018. Gas flow in a multiliquid-
966 inlet rotating packed bed: three-dimensional numerical simulation and internal optimization.
967 Ind. Eng. Chem. Res. 57, 2031-2040.
968 Wu, X., He, M., Yu, Y., Qin, Z., Zhang, Z., 2017. Overall mass transfer coefficient of CO_2
969 absorption in a diameter-varying spray tower. Energy Procedia 114, 1665-1670.
970 Xie, P., 2019. Hydrodynamics and mass transfer of rotating packed beds for CO_2 capture.
971 University of Sheffield.
972 Xie, P., Lu, X., Ding, H., Yang, X., Ingham, D., Ma, L., Pourkashanian, M., 2019. A mesoscale
973 3D CFD analysis of the liquid flow in a rotating packed bed. Chem. Eng. Sci. 199, 528-545.
974 Xu, Y.C., Li, Y.B., Liu, Y.Z., Luo, Y., Chu, G.W., Zhang, L.L., Chen, J.F., 2019. Liquid jet
975 impaction on the single-layer stainless steel wire mesh in a rotating packed bed reactor. AlChE
976 J. 65.
977 Yang, K., Chu, G., Zou, H., Sun, B., Shao, L., Chen, J.F., 2011. Determination of the effective
978 interfacial area in rotating packed bed. Chem. Eng. J. 168, 1377-1382.
979 Yang, W., Wang, Y., Chen, J., Fei, W., 2010. Computational fluid dynamic simulation of fluid
980 flow in a rotating packed bed. Chem. Eng. J. 156, 582-587.
981 Yang, Y., Xiang, Y., Chu, G., Zou, H., Luo, Y., Arowo, M., Chen, J.F., 2015a. A noninvasive
982 X-ray technique for determination of liquid holdup in a rotating packed bed. Chem. Eng. Sci.
983 138, 244-255.
984 Yang, Y., Xiang, Y., Chu, G., Zou, H., Sun, B., Arowo, M., Chen, J.F., 2016. CFD modeling of
985 gas-liquid mass transfer process in a rotating packed bed. Chem. Eng. J. 294, 111-121.
986 Yang, Y., Xiang, Y., Li, Y., Chu, G., Zou, H., Arowo, M., Chen, J., 2015b. 3D CFD modelling
987 and optimization of single-phase flow in rotating packed beds. Can. J. Chem. Eng. 93, 1138-

988 1148.
989 Yi, F., Zou, H.K., Chu, G.W., Shao, L., Chen, J.F., 2009. Modeling and experimental studies
990 on absorption of CO_2 by Benfield solution in rotating packed bed. Chem. Eng. J. 145, 377-384.
991 Ying, J., Eimer, D.A., 2013. Determination and measurements of mass transfer kinetics of CO_2
992 in concentrated aqueous monoethanolamine solutions by a stirred cell. Ind. Eng. Chem. Res.
993 52, 2548-2559.
994 Zhang, G., Ingham, D., Ma, L., Pourkashanian, M., 2022a. Modelling of 3D liquid dispersion
995 in a rotating packed bed using an Eulerian porous medium approach. Chem. Eng. Sci. 250.
996 Zhang, J., 1996. Experiment and modelling of liquid flow and mass transfer in rotating packed
997 bed. Beijing University of Chemical Technology.
998 Zhang, J.P., Luo, Y., Chu, G.W., Sang, L., Liu, Y., Zhang, L.L., Chen, J.F., 2017. A hydrophobic
999 wire mesh for better liquid dispersion in air. Chem. Eng. Sci. 170, 204-212.
1000 Zhang, W., Xie, P., Li, Y., Teng, L., Zhu, J., 2022b. 3D CFD simulation of the liquid flow in a
1001 rotating packed bed with structured wire mesh packing. Chem. Eng. J. 427.
1002 Zhang, W., Xie, P., Li, Y., Zhu, J., 2022c. Modeling of gas-liquid flow in a rotating packed bed
1003 using an Eulerian multi-fluid approach. AlChE J. 68.